Presented at the 40th European Photovoltaic Solar Energy Conference and Exhibition, 18-22 September 2023, Lisbon, Portugal

ANALYSIS OF OPTICAL COUPLING GAINS FROM CELL INTERCONNECTION FOR THE ENERGY RATING OF PV MODULES

Alexander Protti, Anmol Welpulwar, Jibran Shahid, Max Mittag, Ammar Tummalieh, Christian Reichel
Fraunhofer Institute for Solar Energy Systems ISE, Heidenhofstr. 2, 79110 Freiburg, Germany
alexander.aguilar.protti@ise.fraunhofer.de

ABSTRACT: This paper discusses how the geometric design, and the optical properties of the cell interconnection ribbons and wires (CIR) could be adapted for improving the rated yield of PV modules. For such purpose, a comprehensive study of the shading losses and the coupling gains is done for rectangular, round, and triangular CIR cross-section geometries. A sensitivity analysis of the CIR reflectance and geometrical parametrization of each geometry is done with the aid of spectrally resolved raytracing. The impact of the effective width (EW) of the CIR on the rated power, the rated energy yield, and the climate specific energy rating (CSER) of a TOPCon module is then evaluated following the methods for a simulation-based Energy Rating. Results show that improved ribbon reflectance or geometry can enhance module performance by 0.7%. However, the combined effect of better reflectance and geometry can increase the power of a module by 1.6% and the energy yield per area by 1.5%. Furthermore, it is shown that the optical coupling gains can reduce the material consumption of CIR by 15% with still better module performance.
Keywords: Cell Interconnector Ribbons, Effective Width, Optical Coupling Gains, Energy Rating, CTM analysis, Ray Tracing

1 INTRODUCTION

The international standard IEC-61853 series [1] provides the guidelines for determining a rated energy yield [kWh/m²] and a Climate Specific Energy Rating (CSER) of photovoltaic (PV) modules. In the frame of the Ecodesign Directive and the Energy Labelling Regulations, the European Commission [2,3] proposed that manufacturers declare the performance of their modules using the procedures from this standard (IEC-61853), enabling the comparison of PV modules based on the rated energy yield [1], motivating manufacturers to look beyond the rated power [Wp] at standard test conditions (STC) by including the angular, spectral, low-light, and thermal response in the optimization of PV modules.

In a PV module, the cell interconnectors transport the energy from one solar cell to another, enabling the aggregation of voltage and power. The architecture of most solar cells [4] requires the use of cell interconnector ribbons and wires (CIR) which are soldered on top of the busbars and fingers, casting a shadow that reduces the rated power and energy yield from a module [5–7].

For any given number of CIR, decreasing their cross-section area, drops their optical footprint, but increases their electric resistance [5], creating the need for optimization [8,9].

The trend to reduce the finger width and increment the number of ribbons (i.e. busbars) [4] impacts both module reliability and the cell-to-module (CTM) efficiency, due to a redistribution of the ohmic losses in the string connectors [10]. However, a reduction in the cross-section area of each ribbon must follow, so that the sum of all cross-sections remains constant. The resulting spread of the optical footprint from CIR but does not decrease its magnitude.

Therefore, reduction of the shade from CIR requires alternative solutions, such as reflecting the light towards the cell surface (i.e. generating optical coupling gains) [11], shingling the cells [12], or completely removing the metallization from the upper cell surface (i.e. IBC cells). Still, shingled and IBC cells entail challenges that restrict their effectiveness and utilization. Thus, it is expected that CIR be the predominant technology in the market for at least the next decade [4], which creates the urge for maximizing the optical coupling gains from CIR.

Hence, this work explores how the geometry and optical properties of CIR can be adapted for improving the performance of a module. In this search, three main objectives are pursued. First, describe a formal mathematical parametrization of the net shading caused by cell metallization. Second, analyze how the net shading from CIR changes for different geometries, materials, and angles of incidence. Third, estimate the impact of these changes on the module performance, rated power, rated energy yield and Climate Specific Energy Rating.

2 METHODOLOGY

The coupling gains from the CIR can be experimentally determined either by reflection [11] or by light beam induced current (LBIC) [6] measurements. However, none of these methods are used, as in they both require preparation of samples (i.e., mini modules), complementary measurements and/or post processing that might increase the time, cost and uncertainty of the results. Furthermore, the experimental methods in general do not offer better understanding of how the ribbons improve the performance of the modules, which is of relevance for this study.

Therefore, for the current study, a ray tracer model has been developed and optimized for making spectrally resolved simulations for a wide range of CIR geometries. The ray tracer has been integrated into the cell-to-module (CTM) analysis model SmartCalc.Module by Fraunhofer ISE [13].

Other models have been used in studies to analyze the effect of the optical gains from CIR on module power and yield [7,8,14,15]. However, these analysis focus on the net effect (Wp, kWh), offering limited knowledge about the mechanisms inside the module for overcoming the limitations of current ribbon designs. In the following sections a brief explanation complements existing literature [16–18] and helps to better understand the results of the present study. The equations presented in the next

section are compatible with the CTM methodology described in [6,19].

2.1 Optical properties of the CIR

Reflection of light from metals can be defined as specular, with a reflection coefficient described by the Fresnel optics [19]. Models that describe the effect of roughness on the material surface can be found elsewhere [20]. However, for materials with relatively low melting point (such as soldering allows) the coating of the ribbons melts during soldering, leading to a relatively low roughness [21,22]. The fact that most ribbon coatings are produced with a hot-dip process, contributes to this assumption, in case electrically conductive adhesives (ECA) are used. Hence, in the present analysis the roughness of the CIR is not considered, although other studies have made different assumptions [15].

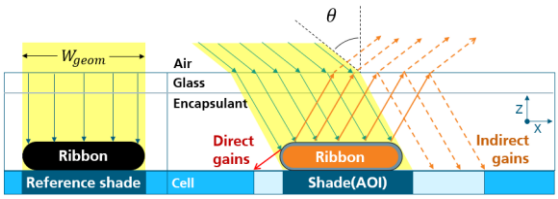

Figure 1: Diagram of the gains and losses of a perfect absorber (left) and a specular-reflecting CIR (right) for a given zenith angle (θ). The geometrical width (W_{geom}) is the width of the shade casted by the perfect absorber, when illuminated from the zenith (θ=0°). Diagram not to scale.

2.2 Mechanisms for generating coupling gains

The coupling gains can be classified in direct or indirect (Fig.1). In an unencapsulated cell, a fraction of the light that hits the metallization is either reflected towards the cell (i.e. direct gains) or absorbed by the metal, while most of the light is reflected away and lost [16]. Nevertheless, when the solar cell is embedded in a module, a fraction of the upwards reflected light is reflected downwards at the glass-air interphase, which increases the probability that it is used to generate electricity (i.e. indirect gains) [17,18]. This reduces the net shading effect of the cell metallization. How much of these indirect gains are achieved by partial or total internal reflection will depend on the angle of incidence (AOI) and the incident light spectrum, as well as the geometry and the optical properties of glass, encapsulant, CIR and cell (reflection, absorption, roughness, texture, etc.).

2.3 Analysis of the coupling gains

In the field of CTM analysis, the level of optical coupling caused by a "shading object" (busbar, finger or ribbon) can be parametrized in terms of the "effective width" (EW) [6,11], which is the complement of the "transparency" [15]:

$$EW = 1 - Transparency \quad (1)$$

Although, most readers might find the concept of "transparency" more intuitive to understand than the EW, the latter is easier to use in CTM analysis calculations and is always a positive value. Hence, it is explained in further detail in the next section.

2.4 The effective width (EW)

The EW indicates the normalized net shading loss after accounting for any reflection gains. Mathematically, this is the difference between the shaded flux (losses) [W] and the recovered flux (gains) [W] normalized by the shade caused by a perfect absorber (zero reflectance) with the same geometry, when illuminated from the zenith ("reference shade") (Fig.1). For a given pair of zenith (θ) and azimuth (ϕ) angles, the EW is the difference between normalized shade and normalized gains:

$$EW(\theta,\phi) = \frac{net\ shade(\theta,\phi)}{reference\ shade} \quad (2a)$$

$$EW(\theta,\phi) = \frac{shade(\theta,\phi) - gains(\theta,\phi)}{shade(0°,\phi)} \quad (2b)$$

$$EW(\theta,\phi) = normalized\ shade - normalized\ gains \quad (2c)$$

An ideal "coupling object" would have an EW=0%, as all the light would be always optimally redirected to the cell. The opposite would be an EW=100% at an AOI=0°, which then increases for AOI>0, as the shade covers a wider cell area, but no shaded light is recovered ($W_{shade} > W_{geom}$).

The angular shade and gains, depend not only on the AOI, but also on the spectral distribution of the incoming light, the geometry, and optical properties (refractive index, extinction coefficient) of the shading object and the module layers. The optical properties of the cell (reflectance, spectral response, texture, angular response, etc.) affect the EW as well.

2.5 Effective shade

In the case of a full-squared solar cell, the effective shade (ES) casted by a shading object with a given geometrical width (W_{geom}) and length (L_{geom}), can be defined as:

$$ES_i(\theta,\phi) = EW_i(\theta,\phi) * W_{i,geom} * L_{i,geom} * N \quad (3)$$

Here, N is the number of elements of one type of shading object i which can cause optical couplings, such as fingers (F), busbars (BB), or CIR.

2.6 Net shading loss from CIR

The following equation exemplifies the use of the ES for obtaining the "net fractional reduction in cell illumination caused by the CIR after encapsulation" (k_{CIR}):

$$k_{CIR} = \frac{A_{cell,geom} - ES_{F,encaps} - ES_{CIR/BB,encaps}}{A_{cell,geom} - ES_{F,encaps} - ES_{BB,encaps}} \quad (4)$$

Here, the subindex "CIR/BB" indicates that the CIR is placed on top of the busbar and both objects are accounted as one. The subindices "$encaps$" and "air" indicate whether the cell is encapsulated or not. In the case of a full square cell, the geometrical area of the cell can be obtained by the product of its length and width ($A_{cell,geom} = W_{geom,cell} * L_{geom,cell}$).

2.7 Incidence angle modifier

The incidence angle modifier describes the angular dependency of the short circuit current (Isc) of a module at given zenith (θ) and azimuth (ϕ) angles with respect to the Isc at zenithal irradiance:

$$IAM(\theta,\phi) = \frac{Isc(\theta,\phi)}{Isc(0,\phi)} \quad (5)$$

The EW behaves differently for each azimuth angle [15], which impacts the IAM. In such case, as specified in [1], the IAM of the module should be measured at two perpendicular azimuth angles ϕ_1 and $\phi_2 = \phi_1 + 90$. In the current analysis, the average of those values is considered for the virtual energy rating calculations:

$$IAM(\theta) = \frac{IAM(\theta,\phi_1) + IAM(\theta,\phi_2)}{Isc(0,\phi)} \quad (6)$$

3 VARIATION OF THE EW WITH RESPECT TO THE ANGLE OF INCIDENCE

In this section, the AOI is defined as the zenith angle of the incidence light on the glass, before refraction takes place, when the azimuth is parallel to the x coordinate (Fig.1). This direction is where the net shade is most sensitive to changes in the cross-section geometry of the shading object.

Since most used CIR nowadays are round wires, the angular dependency of the EW is exemplified for unitary height-to-width ratio (H/W=1). This is displayed in figures 2, 3 and 4 for square, round, and triangular CIR, where the black line represents the normalized shade, and the green line, the sum of both direct and indirect gains. The difference between the green and black line is the EW.

In the case of the square ribbon (Fig.2), the EW has a value of 100% at AOI=0° because all the light that hits the ribbon is reflected outside of the module. The direct gains increase proportional to the shaded area, which depends on the AOI (notice the symmetry in the gray shade and the red gains in Fig.2 upper right). The angular dependency of the indirect gains is described by the angular reflection on the glass-air surface (Fresnel's equations). So, light that hits the glass at an AOI close to 90° will be refracted inside the module almost at the critical angle. Since the horizontal surface of the ribbon is parallel to the glass surface, when the AOI is close to 90°, the indirect gains approach total internal reflection, reducing the EW. From this analysis derives the following conclusion: increasing the H/W ratio increases both normalized shade and direct gains but reduces the indirect gains.

For the round ribbon (Fig.3), there is an overlapping of indirect and indirect gains on the cell surface, because light is reflected in all directions. For an AOI=0°, the upper half of the ribbon surface is responsible for indirect reflection. However, the parts of the CIR surface with tilts greater than 45° (both left and right) reflect the light downwards, causing direct gains. As the AOI increases, the ratio between direct and indirect gains, as well as the EW remain practically constant. Still, changing the H/W ratio has a similar effect as described before for the rectangular ribbon.

In the case of the triangular ribbon whose tilt is greater than 45° (Fig.4), there is a transition from direct to indirect coupling gains when the refracted angle (AOI_{inner}) is greater than a certain threshold ($AOI_{inner} > 2 * tilt - 90°$). For monochromatic light, this transition would cause a discontinuity in the EW. However, for polychromatic light, the transition takes place gradually (i.e. for a given AOI only a fraction of the spectrum is reflected close to horizontally). Furthermore, the shade of the ribbon increases when $AOI_{inner} > 90° - tilt$. For extremely flat (H/W<<1) or wide (H/W>>1) ribbons, the tendencies described for rectangular ribbons with respect to the H/W apply. In all cases, both direct and indirect gains decrease proportional to the reflectance of the CIR coating.

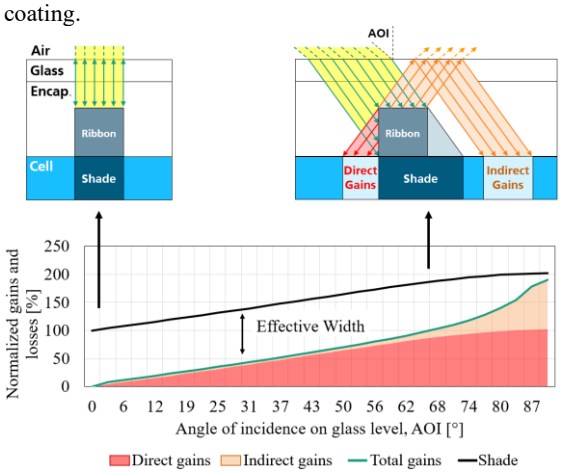

Figure 2: Angular behavior of the coupling gains, losses and effective width for a perfectly specular reflecting cell interconnector with a square cross-section area.

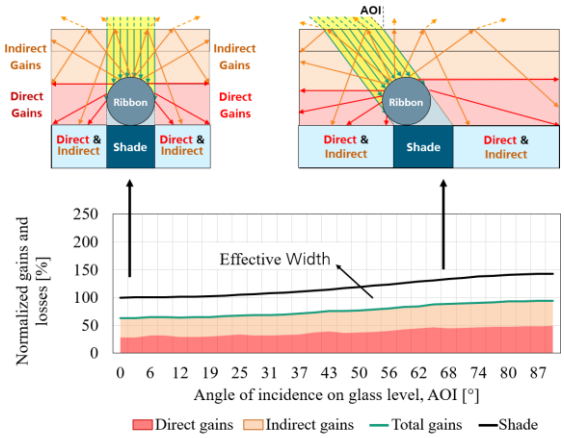

Figure 3: Angular behavior of the coupling gains, losses and effective width for a perfectly specular reflecting cell interconnector with a round cross-section area.

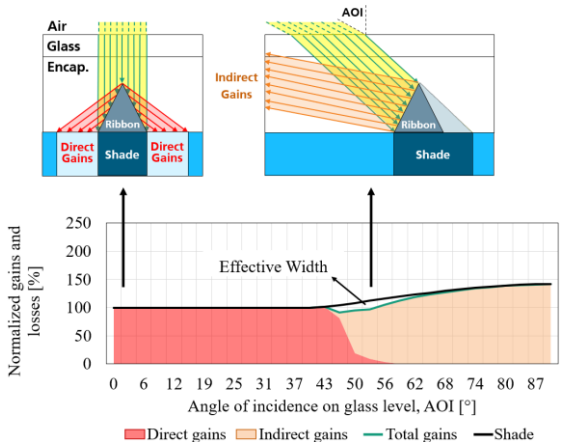

Figure 4: Angular behavior of the coupling gains, losses and effective width for a perfectly specular reflecting cell interconnector with a triangular cross-section area, with a unitary heigth-width ratio (H/W=1) and a tilt of 63.4°.

4 IMPACT OF THE EW ON MODULE PERFORMANCE

To evaluate the impact on module performance of different CIR designs, the module characteristics listed in the Table below are considered. In all cases, the reference ribbon is a tin-lead coated (Sn63Pb37, abbreviated as SnPb for simplicity) round wire, with a copper core and a diameter of 300 µm, which is widely used in current PV modules [4].

Table I: Characteristics of the simulated module

Layout	Cell spacing: 2mm String spacing: 2mm Margins: 21mm Number of cells: 120 Module length = 2.18 m Module width = 1.31 m Module area = 2.856 m²
Cell	Cell type: half-cut M12 TOPCon Efficiency = 24.4% Bifaciality = 83% $W_{F,geom}$ width = 0.05mm $W_{BB,geom}$ width = 0.05mm N_F = 60 (front) / 69 (rear) N_{BB} = 18
Cover	Front: 2.0 mm clear glass with ARC Rear: 2.0 mm clear glass with ARC
Encapsulant	Front: UV transmitting EVA Rear: UV blocking EVA Thickness = 600 µm
Cell interconnectors	Resistivity = 1.8 µΩ-cm Dimensions: see table II
String interconnectors	Resistivity = 1.8 µΩ-cm Width = 5.072 mm Thickness = 0.472 mm
Junction box	Number: 2 Internal resistance = 0.03 mΩ
Cables	Length = 0.5 m Cross section = 4 mm² Specific resistance = 0.02 Ω-mm²/m Contact resistance plug/jack=0.3mΩ

4.1 Variation of the ribbon reflectance

The effect of the reflecting properties of the coating is studied by virtually changing the refractive index and extinction coefficient of the reference ribbon (tin-lead-solder alloy (Sn63Pb37)) to that of copper (Cu), aluminum (Al) and silver (Ag). In all cases, a width of 300 µm and an area of 0.071 mm² is used (see Table II).

The results are summarized in Figure 5. Here, for all geometries, the reference ribbon (blue) has the lowest power, energy yield and energy rating, while silver (green bar) presents consistently the highest values. In the case of the round ribbon, a silver coating can increase the power and yield of the module by 0.7%. That is 4.2 Wp or 2.2 kWh/m². Coating materials such as Al and Cu cause intermediate effects.

This relative behavior between the coatings is due to the differences in the spectral and angular reflectance of the different materials (see Fig.6). Here the spectral response is included to highlight the relative importance of the reflectance in each wavelength. The tin-lead solder alloy has overall the lowest reflectance, which is similar to copper for wavelengths below 600 nm. At greater wavelengths, copper has a remarkably better reflectance. In the case of aluminum, it is overall a better reflector than copper, but at around 600 nm is outperformed by copper. Silver behaves almost as a perfect reflector for wavelengths greater than 500 nm.

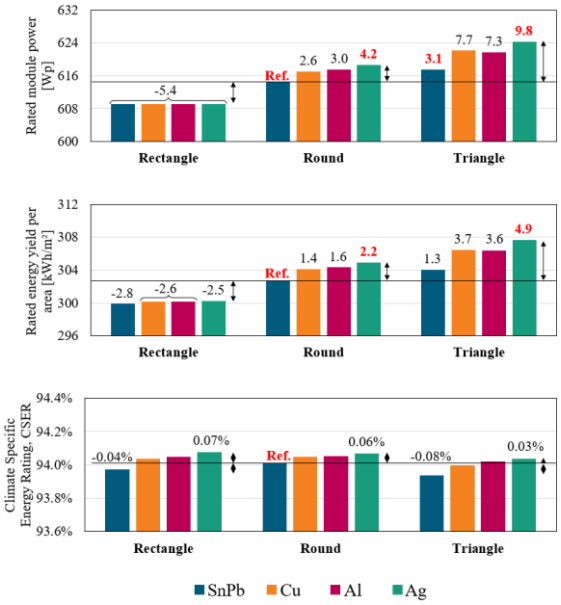

Figure 5: Effect of the coating and shape of the ribbon on the module performance

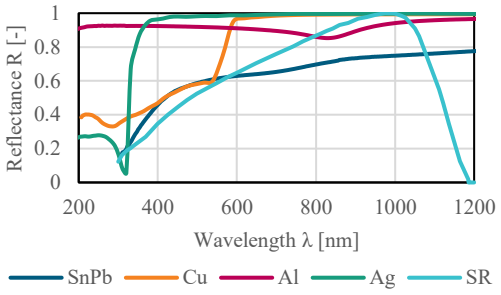

Figure 6: Spectral reflectance of tin-lead (SnPb), copper (Cu) aluminum (Al) and silver (Ag) coatings different coating materials for a normal incident angle. A normalized spectral response (SR) is included to illustrate the relative relevance of each reflected wavelength on the optical gains.

4.2 Variation of the ribbon shape

Figure 5 shows that rectangular ribbons cause a reduction of 5.4 Wp (-0.88%) and 2.8 kWh/m² (-0.92%) in module performance. On the other hand, changing the shape from round to triangular, causes an increment of 3.1 Wp (0.5%) and 1.3 kWh/m² (0.4%) in module power and yield per area, respectively, without changing the ribbon coating. However, a combination of using silver on triangular-shaped ribbons causes an increment of almost 9.8 Wp (1.6%) and 4.9 kWh/m² (1.5%) with respect to the reference.

Whenever the shape or the coating are changed, the ER remains practically constant because power and yield are increased in a similar proportion.

Table II: Area, height and height-to-width ratio (H/W) of analyzed ribbon shapes with a width of 300 µm

Area, mm²	Height, µm			H/W (Tilt, °)		
	■	▲	●	■	▲	●
0.045	150	**300**	191	0.50	**1.00 (63.4°)**	0.64
0.060	200	400	255	0.67	1.33 (69.4°)	0.85
0.071	236	471	**300**	0.79	1.57 (72.3°)	**1.00**
0.090	**300**	600	382	**1.00**	2.00 (76.0°)	1.27

4.3 Variation of the ribbon cross-section area and aspect ratio

The variations in the ribbon cross-section were done using the dimension showed in Table II. Figure 7 shows that power and yield improve with greater ribbon cross-section area, because the ohmic resistance decreases. This is not that important under low-light irradiance because the resistive losses decrease with the square of the current ($\Delta P=R*I^2$). Therefore, changes in module power due to reduced series resistance are relatively greater than the improvements in module yield, which explain the decreasing trend in the CSER with respect to the cross-section area. Still, the coupling gains of triangular ribbons can improve module power, yield and ER, even when the cross-section area of the ribbon is reduced by 15% (from 0,07 to 0,06 mm²).

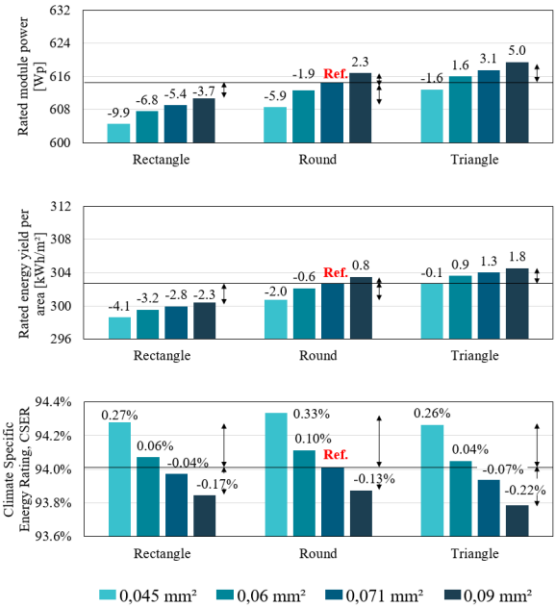

Figure 7: Effect of the cross section area and shape of the ribbon on module performance

5 CONCLUSION

A formal mathematical description of the optical coupling gains of cell interconnector ribbons was presented in this study. An analytical explanation of the angular behavior of the EW for different ribbon shapes elucidated the benefits of using triangular ribbons with H/W>1. Furthermore, the values presented here work as first approximations when performing cell-to-module (CTM) analysis under STC and non-STC conditions, simplifying the acquisition of data for CTM analysis.

The impact of different ribbons geometries was studied for different performance indicators, including the energy rating. It was shown that the optical coupling gains not only can improve module power, rated energy yield and energy rating, but also allow saving of ribbon material.

6 ACKNOWLEDGEMENT

This work was supported by the Federal Ministry for Economics and Climate Action (BMWK) under contract number 03EE1045B, with the acronym SMART.

7 REFERENCES

[1] International Electrotechnical Commission, Photovoltaic (PV) module performance testing and energy rating – Part 4: Standard reference climatic profiles, 1st ed., IEC Central Office, Geneva, Switzerland, 2018.

[2] A. Wade, et al., The Product Environmental Footprint (PEF) of photovoltaic modules-Lessons learned from the environmental footprint pilot phase on the way to a single market for green products in the European Union, Prog Photovolt Res Appl 26 (2018) 553–564. https://doi.org/10.1002/pip.2956.

[3] N. Dodd, N. Espinosa, Preparatory study for solar photovoltaic modules, inverters and systems, 2019.

[4] ITRPV, International Technology Roadmap for Photovoltaic (ITRPV): 2022 Results, fourteenth ed., 2023.

[5] H. Hanifi, et al., Investigation of cell-to-module (CTM) ratios of PV modules by analysis of loss and gain mechanisms, Photovoltaics International (2016) 89–99.

[6] I. Hädrich, Unified methodology for determining CTM ratios: Systematic prediction of module power, in: Proceedings of the 4th International Conference on Crystalline Silicon Photovoltaics, 's-Hertogenbosch, Netherlands, 2014.

[7] M. Mittag, et al., Triangular ribbons for improved module efficiency, in: Proceedings of the 32nd European Photovoltaic Solar Energy Conference and Exhibition, Munich, Germany, 2016, pp. 169–172.

[8] H. Hanifi, et al., Optimized tab width in half-cell modules, Enrgy Proced 92 (2016) 52–59. https://doi.org/10.1016/j.egypro.2016.07.009.

[9] A. Protti, J. Shahid, M. Mittag, D. H. Neuhaus, U. Kräling, M. Kaiser, Virtual Energy Rating: a method for optimizin module performance through cell-to-module analysis.

[10] Student Awards Finalist Presentation: Impact of String Connection and Contact Degradation on Electrical Current Distribution on Solar Cell and Photovoltaic Module Level: a Magnetic Field Imaging Validated Model, 2023.

[11] I. Hädrich, et al., Finger and ribbon optics for increasing module power, in: Proceedings of the 31st European Photovoltaic Solar Energy Conference and Exhibition, Hamburg, Germany, 2015.

[12] M. Mittag, et al., Cell-to-Module (CTM) Analysis for Photovoltaic Modules with Shingled Solar

Cells, in: 2017 IEEE 44th Photovoltaic Specialist Conference (PVSC), Washington, DC, IEEE, 25.06.2017 - 30.06.2017, pp. 1531–1536.

[13] Fraunhofer Institute for Solar Energy Systems ISE, SmartCalc.Module. http://www.cell-to-module.com (accessed 1 September 2023).

[14] I. Haedrich, M. Ernst, Impact of Optimizing Cell Metallization for Local Conditions on the Module Energy Yield, in: 2021 IEEE 48th Photovoltaic Specialists Conference (PVSC), Fort Lauderdale, FL, USA, IEEE, 2021, pp. 2104–2110.

[15] I. Haedrich, M. Ernst, Impact of angular irradiance distributions on coupling gains and energy yield of cell interconnection designs in silicon solar modules in tracking and fixed systems, J. Phys. D: Appl. Phys. 54 (2021) 224003. https://doi.org/10.1088/1361-6463/abe967.

[16] R. Woehl, M. Hoerteis, S.W. Glunz, Analysis of the Optical Properties of Screen-Printed and Aerosol-Printed and Plated Fingers of Silicon Solar Cells, Advances in OptoElectronics 2008 (2008).

[17] M.F. Stuckings, A.W. Blakers, A study of shading and resistive loss from the fingers of encapsulated solar cells, Sol Energ Mat Sol C 59 (1999) 233–242. https://doi.org/10.1016/S0927-0248(99)00024-0.

[18] A.W. Blakers, Shading losses of solar-cell metal grids, Journal of Applied Physics 71 (1992) 5237–5241. https://doi.org/10.1063/1.350580.

[19] F.L. Pedrotti, Optik für Ingenieure: Grundlagen ; mit 28 Tabellen, third., bearb. und aktualisierte Aufl., Springer, Berlin [u.a.], 2005.

[20] Matt Pharr, Wenzel Jakob, Greg Humphreys, Physically Based Rendering: From Theory To Implementation, 2023. https://pbr-book.org/.

[21] R. Meier, et al., Microstructural Optimization Approach of Solar Cell Interconnectors Fatigue Behavior for Enhanced Module Lifetime in Extreme Climates, Energy Procedia 92 (2016) 560–568. https://doi.org/10.1016/j.egypro.2016.07.020.

[22] Tae-Sik Cho, Chul-Sik Cho, Enhancement of the Surface Smoothness of Cu Ribbon for Solar Cell Modules 16 (2015).